Transient oxygenation of the Mediterranean after the Zanclean megaflood

Udara Amarathunga[a,b,1] (ID), Jochen J. Brocks[b] (ID), Paul Th. Meijer[c] (ID), Janet M. Hope[b], Willem-Jan Zachariasse[c], Rick Hennekam[d] (ID), Isabel van der Hoeven[d] (ID), Ursula Roehl[e] (ID), Susan Rule[f], Ulrike Troitzsch[g] (ID), Simon Haberle[f,h] (ID), Appy Sluijs[c] (ID), Katharine M. Grant[b], Wout Krijgsman[c], Daniel Garcia-Castellanos[i], Andrew McC. Hogg[b,j] (ID), Gert-Jan Reichart[c,d] (ID), Andrew P. Roberts[b], and Eelco J. Rohling[c,k]

Affiliations are included on p. 8.

The Mediterranean basin reconnected to the Atlantic Ocean ~5.33 Myr ago, following its partial desiccation during the preceding Messinian salinity crisis (5.97 to 5.33 Myr). While the extent of terminal Messinian drawdown and abruptness of reconnection are debated, recent work inferred that an anomalously long-lasting eastern Mediterranean organic-rich "mystery sapropel" layer was deposited due to salinity-stratification and anoxia following catastrophic flooding that refilled the basin. However, independent evidence is required to test this hypothesis. Here, we present extensive proxy data and numerical model results to show that irrespective of the largely hypersaline or oligohaline conditions proposed for the terminal Messinian, the eastern Mediterranean became oxygenated due to the ~1.5-km-high, turbulent and aerated cascade that refilled the basin, which created a salinity-stratified but oxygenated water column that allowed preservation of only the most recalcitrant organic components. Next, oxygen was gradually depleted over a period of up to 12,000 y due to remineralization of sinking organic matter, culminating in a stratified, anoxic basin. It took 33,000 y after flooding (7,000 y longer than suggested previously) for turbulent diffusion to weaken the stratification and allow resumption of convective deep-water renewal, which marked the final return of normal oxygenated marine conditions throughout the Mediterranean.

Messinian salinity crisis | Mediterranean | Zanclean megaflood | sapropels

Late Miocene tectonic restriction of the Atlantic–Mediterranean gateway resulted in partial desiccation of the Mediterranean basin (Messinian salinity crisis; MSC, 5.97 to 5.33 Myr ago) (1–4). During the peak MSC (5.6 to 5.52 Myr), both western and eastern Mediterranean basins underwent kilometer-scale drawdowns, leading to giant evaporite deposit formation (1, 2, 4–6). Evidence for a massive drawdown comes from a basin-wide Messinian erosional surface and deep canyons beneath major river mouths such as the Nile and Rhone rivers (2, 4, 7). The extent of intrabasin connectivity and environmental conditions following the peak MSC are uncertain (1, 8), which complicates understanding of the nature and timescales of Mediterranean refilling at the Miocene/Pliocene boundary (5.33 Myr).

The abruptness of Atlantic–Mediterranean reconnection is estimated from the latest Messinian drawdown magnitude of Mediterranean subbasins. Paleontological and biogeochemical evidence imply intermittently brackish biotic associations and Messinian brine dilution with Paratethyan and riverine influx following the peak MSC across Mediterranean subbasins, which may suggest an elevated terminal Messinian sea-level during the final MSC phase (5.52 to 5.33 Myr) (9–11). Based on this evidence for brackish water conditions, an outflow pump mechanism forced by density-driven Paratethys inflow was suggested to explain MSC termination (12). Moreover, alkenone-based paleoproxy records have been used to suggest a progressive return to marine conditions in western Mediterranean marginal basins due to gradual Atlantic influx following the peak MSC (13). In contrast, seismic data and sedimentological observations imply that the Mediterranean was largely drawn down and isolated from the Atlantic Ocean and other major water bodies up to MSC termination at the Miocene–Pliocene boundary when the Gibraltar gateway reopened (4, 14–16). For an eastern Mediterranean base level that was drawn down by ~2 km (2, 4, 17), Gibraltar sill collapse at the MSC termination would have generated the most abrupt flooding event in recorded Earth history, termed the Zanclean megaflood (2, 4). However, despite five decades of research, the drawdown magnitude during the terminal MSC and the consequences of basin refill remain debated (2, 9, 18).

Significance

The Mediterranean basin was isolated from the Atlantic Ocean (at ~6 Myr), causing a kilometer-scale evaporative drawdown during the Messinian salinity crisis (MSC). The Mediterranean configuration immediately before Atlantic reconnection (5.33 Myr) is debated, with opposing views of a largely refilled brackish-water basin *versus* a persistently partially desiccated basin. Using geochemical data and numerical models, we show that an abrupt flood ended the MSC, causing eastern Mediterranean salinity stratification and oxygenation. Oxygen consumption by remineralization caused subsequent anoxia, while an anomalous organic-rich layer was deposited until deep convection ended the 33,000-y stratification phase. Our study supports the megaflood hypothesis, where the most abrupt flooding event in recorded geological history terminated the MSC from a substantially drawn-down state before Atlantic reconnection.

The presence of an anomalously long-lasting eastern Mediterranean organic-rich layer (26,000 y; mystery sapropel) immediately following the M/P boundary has been linked to MSC termination mechanisms. It has long been established that Mediterranean sapropels formed during Northern Hemispheric precession minima (insolation maxima), due to curtailed deep water formation during extensive monsoon flooding phases into the Mediterranean (19–21). However, the mystery sapropel at eastern Mediterranean Ocean Drilling Program (ODP) Site 967 spans the first two Pliocene insolation maxima and the intervening insolation minimum, based on Ba abundances (2), a proxy for organic carbon deposition that is resilient to postdepositional oxidation (22–24). It is the only sapropel to span more than one insolation maximum in the entire Neogene, implying a forcing other than climate and suggesting a relation with MSC termination (2). It was hypothesized that the eastern Mediterranean was salinity-stratified due to an abrupt flooding event that terminated the MSC, triggering a lengthy phase of deep-water anoxia and mystery sapropel deposition, before the reestablishment of normal marine conditions (2).

While eastern basin salinity stratification was proposed to result from remnant brine transfer from the western Mediterranean, an alternative scenario has not yet been evaluated that foresees Mediterranean subbasin flooding under largely oligohaline conditions. Moreover, independent evidence on the salinity stratification mechanism is required to validate a megaflood-driven MSC termination. Therefore, we test possible Mediterranean geochemical configurations that allow the observed sapropel deposition patterns, considering a range of largely hypersaline to largely oligohaline conditions before the Atlantic reconnection. At ODP Site 967, all sapropels older than 3.2 Myr have been degraded due to postdepositional oxidation (*SI Appendix*, Fig. S1), which hinders a detailed study of the mystery sapropel (2, 25, 26). At ODP Site 969, Early Pliocene sapropels are well preserved, allowing detailed analysis of a mystery sapropel equivalent from the Mediterranean Ridge crest (27) (Fig. 1). We combine high-resolution geochemical data from X-ray fluorescence core scanning (XRF-CS) and complementary organic carbon, mineralogical, and organic biomarker data for the mystery sapropel at eastern Mediterranean ODP 969, with numerical modeling of deep-water oxygenation, to obtain a detailed characterization of this enigmatic final phase immediately following the Mediterranean Zanclean megaflood.

Results

Mystery Sapropel Data. The Site 969 mystery sapropel is ~1 m thick and consists of two clear dark bands within a laminated, olive-gray background (Fig. 1). Our XRF-CS results reveal two Ba peaks that correspond to the dark bands, with low Ba levels between the peaks. However, organic carbon quantification indicates that, while the normal sapropel-like Ba peaks indicate high organic carbon contents exceeding 1.7 %, elevated levels (>1.0 %) continue between these peaks, and are substantially higher than the ~0.3% organic matter content of intervening nonsapropelic eastern Mediterranean marls (28). Thus, we suggest that the Ba peaks correspond to the first two Pliocene insolation maxima, while the intercalated low Ba–high organic carbon values represent nonsapropelic preservation during the intervening insolation minimum. Oxygen isotope data ($\delta^{18}O$) provide further support for this interpretation, where the first two Pliocene $\delta^{18}O$ minima are concurrent with the two Ba peaks(29). Our chronology based on this assumption is consistent with a reevaluated biostratigraphy for Site 969 (*Materials and Methods*) and indicates that enhanced organic carbon preservation extended to the second Pliocene insolation minimum (*SI Appendix*, Fig. S2
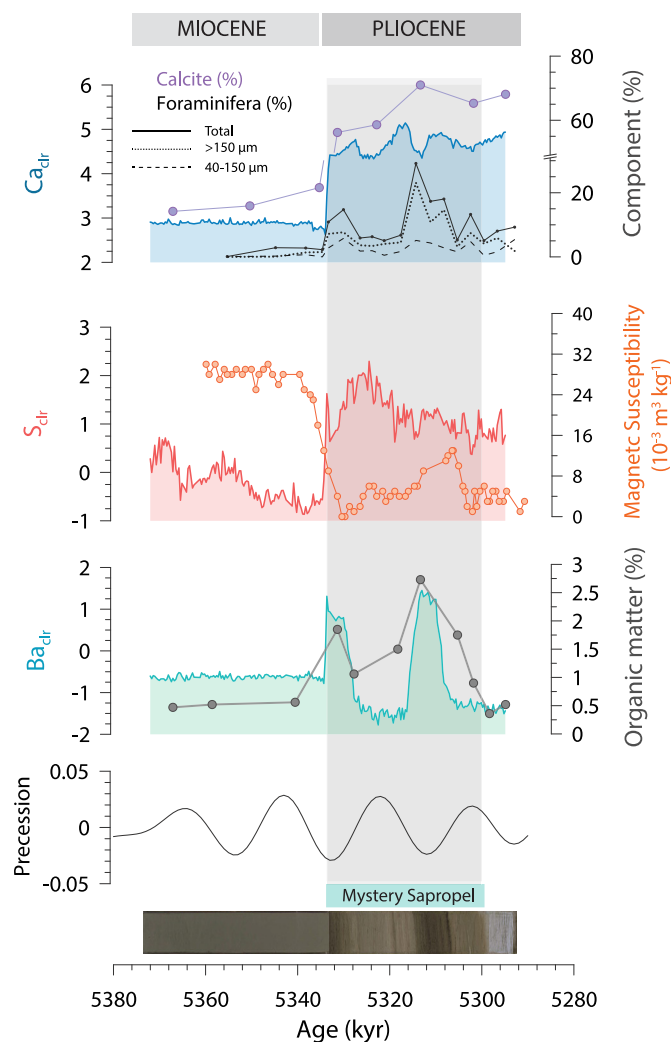
Fig. 1. XRF core scanning, XRD, and organic matter data across the Miocene/Pliocene boundary from ODP Site 969. The age model was developed by tuning Ba peaks to 65°N insolation maxima and was validated using biostratigraphy (*Materials and Methods* and *SI Appendix*, Fig. S2). The M/P boundary is marked by a rapid Ca (mainly calcite) concentration increase. Foraminifera shell abundance data(27) suggest that the Ca increase is predominantly due to the influx of planktonic foraminifera to the Mediterranean. The mystery sapropel interval consists of two dark olive-gray layers within an olive-green background. The two dark layers correspond to the first two Pliocene Ba peaks. Organic carbon concentration is >1 % within the mystery sapropel. High S contents above the M/P boundary are mainly caused by elevated gypsum contents, while the magnetic susceptibility trend is reflected by pyrite contents(27) (*SI Appendix*, Fig. S3).

and Table S1). Therefore, mystery sapropel deposition may have continued for ~33,000 y (about 1.5 precession cycles); ~7,000 y longer than estimated previously (2).

The calcite content rises to ~60% immediately after the M/P boundary, from values as low as 20% in the latest Messinian. While benthic foraminifera are absent within the mystery sapropel, planktonic foraminiferal abundance increases 4 to 5-fold simultaneously (dominantly due to an increase in the >150 μm fraction), which explains the calcite increase due to Atlantic water influx (Fig. 1 and *SI Appendix*, Table S2). Sulfur (S) contents within the first half-precession cycle above the M/P boundary are considerably higher (XRF-CS intensities increase up to fivefold) than in the rest of the mystery sapropel (Fig. 1). However, magnetic susceptibility measurements indicate a reverse pattern, with the lowest values within the first Ba peak that rise to higher values in the second Ba peak. In general, higher than background

magnetic susceptibility values within sapropels correlate with elevated sedimentary pyrite contents (20). This observation is consistent with X-ray diffraction (XRD) data, which indicates declining pyrite contents across the M/P boundary, which rise to Messinian values within the second Ba peak (*SI Appendix*, Fig. S3). Our XRD data indicate that higher S contents are most likely caused by elevated gypsum contents (also, possible anhydrite) rather than pyrite contents in the sediment immediately above the M/P boundary (*SI Appendix*, Fig. S3).

Smear-slide analysis reveals abundant latest Messinian gypsum twin crystals at Site 969, which suggests its authigenic precipitation through the water column (27, 30). However, twin crystal abundance decreases across the M/P boundary, becoming rare within mystery sapropel sediments (27). Our observations of gypsum enclosing and infilling foraminiferal shells in the basal Pliocene suggest a higher percentage of postdepositional/diagenetic precipitation (*SI Appendix*, Fig. S4). Likely causes of gypsum precipitation include 1) elevated bottom salinities due to remnant Messinian fluids (consistent with abundant late Messinian twin crystals), or 2) postdepositional pyrite oxidation under anaerobic or aerobic conditions (31). Importantly, the pyrite/organic carbon ratio drops above the M/P boundary (unlike normal sapropels, where pyrite maxima correlate with high organic carbon), which is suggestive of a largely oxygenated water column (32, 33). Vertical oxygen diffusion through the sediment–water interface may explain the high gypsum abundance coincident with diminished pyrite contents above the M/P boundary, which suggests a Mediterranean water column redox condition shift.

Postflood Eastern Mediterranean Oxygenation. Our biomarker and pollen data provide evidence for Late Messinian stratification, postflood water column oxygenation, and a return to largely anoxic basin conditions within 8 to 12 thousand year (Fig. 2 *A–D*). Before Atlantic–Mediterranean reconnection, elevated relative archaeol, gammacerane, and tetrahymanol concentrations (Fig. 2*A*) suggest stratified Mediterranean conditions (34). Relative abundances of these biomarkers drop rapidly toward zero at the M/P boundary, coincident with Atlantic reopening, cessation of Messinian hypersaline conditions, and initiation of seafloor algal and plant biomass flux. The high archaeol abundance may indicate highly saline conditions, consistent with abundant latest Messinian gypsum twin crystals (27, 34). However, this is not a definitive high-salinity indicator, as archaeol has been observed in euxinic environments such as the Black Sea where hypersaline conditions are not present (35).

Notable relative abundance changes of algal and plant lipid classes support our hypothesis of a major long-term water column redox condition shift from the first to second barium maximum. The relative lipid biomarker abundance in nonsapropelic Pliocene sediments is substantially lower compared to that of Pliocene sapropels, due to oxic degradation of organic matter in the water column or to oxygen diffusion into the sediment (36). Accordingly, the lipid profile of the younger Ba peak points to minimal organic carbon reworking typical of Pliocene sapropels (36) (Fig. 2 and *SI Appendix*, Table S2). By comparison, sediments within the first Ba peak are strongly depleted in labile phytoplankton lipids and enriched in recalcitrant terrestrial vegetation biomarkers indicative of more intensive degradation under aerobic conditions. Notably, the C26:0 over C18:0 FA ratio is depressed in the first Ba peak relative to the second (Fig. 2*B*), which is typical of aerobic reworking (37). Similarly, the alcohol preference index (API) that demarcates n-alcohol degradation relative to more recalcitrant n-alkanes (38) (Fig. 2*B*), the relative abundance of FA over less labile n-alcohols (36), algal dinosterol over more recalcitrant land
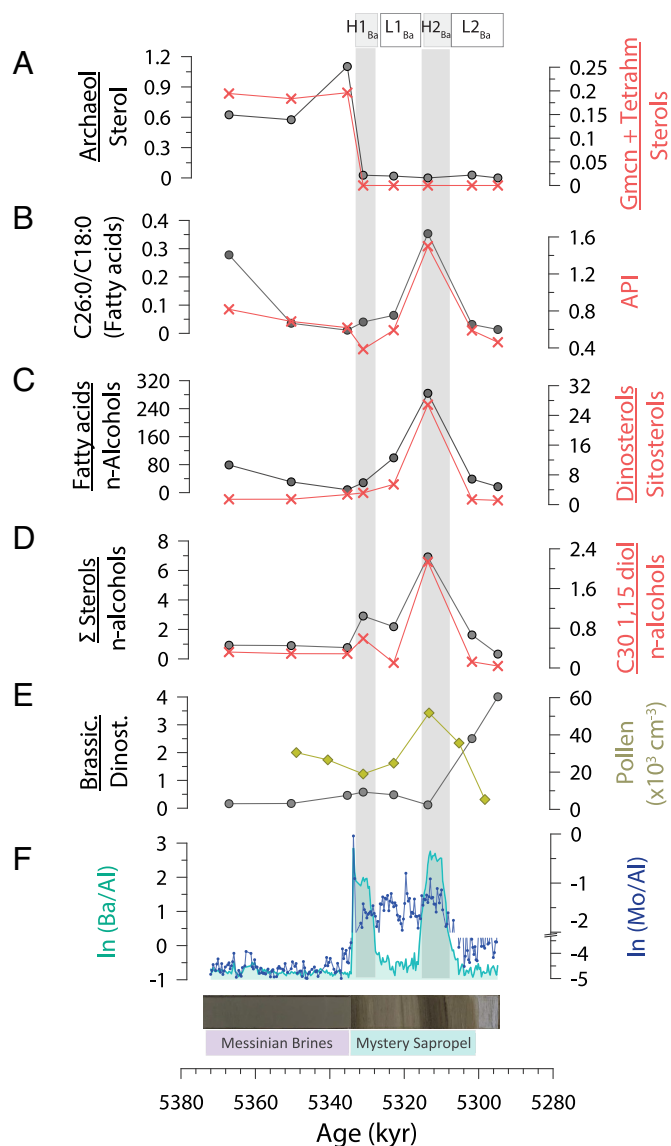
Fig. 2. XRF, biomarker, and pollen data indicating a gradual transition from a largely oxidizing to a reducing eastern Mediterranean water column. (*A*) Relative archaeol, gammacerane, and tetrahymanol abundances normalized to sterol content (*SI Appendix*, Table S3). (*B*) Relative abundance of C26:0 and C18:0 fatty acids (FA) and alcohol preference index (*Materials and Methods*). (*C*) FA/n-alcohol and dinosterol/sitosterol ratios. (*D*) Total sterols/n-alcohols and C30 1,15 diol/n-alcohol ratios. (*E*) Brassicasterol/dinosterol ratio and pollen content. (*F*) Mo/Al and Ba concentration. While Messinian biomarkers indicate anoxic conditions, Mo/Al values are low, indicating diminished Atlantic inflow. Mo/Al is lowest in the first mystery sapropel Ba peak, implying higher water column O2. The Ba/Al ratio is plotted to show high and low Ba regions through the mystery sapropel. H1$_{Ba}$, H2$_{Ba}$ (shaded in light gray) and L1$_{Ba}$, L2$_{Ba}$ are high and low barium regions, respectively. See *SI Appendix*, Table S3 for explanation of all biomarker ratios.

plant-derived sitosterol (Fig. 2*C*), and the abundance of total sterols and C30 1,15-diol over relatively more stable n-alcohols (36, 37) (Fig. 2*D*) increase markedly toward the younger Ba peak. More intense aerobic organic carbon reworking during deposition of the first Ba peak is also supported by an up to three times lower pollen count in the first Ba peak compared to the second (39) (Fig. 2*E*). These combined data indicate a more oxygenated water column during the first ~8 to 12,000 y of mystery sapropel formation, followed by a shift to more reducing conditions typical of younger sapropels. The end of mystery sapropel deposition is marked by a sharp rise of (epi)brassicasterol abundances relative to dinosterol, which points to a possible shift from dinoflagellates

to haptophytes (or possibly diatoms) as the dominant phytoplankton (40) (Fig. 2*E*).

Evidence for a major seawater influx comes from Site 969 Mo data (Fig. 2*F*). In isolated anoxic basins with relatively little water influx from a surrounding ocean, Mo will be depleted compared to the global ocean, due to sedimentary Mo enrichment (41, 42), so that little Mo would have remained in Messinian waters. We, thus, interpret the Mo/Al increase immediately above the M/P boundary to reflect a sudden Mo-bearing Atlantic water influx to the eastern Mediterranean. Sedimentary Mo enrichment is observed commonly in euxinic settings, where water column MoO_4^{2-} is converted into thiomolybdate species in the presence of hydrogen sulfide, which is permanently buried in sediment (41, 42). Mo/Al is lowest in the first Ba peak, and steadily rises in the second Ba peak, which suggests that water column conditions became more reducing from the first and into the second Ba peak, consistent with our biomarker data. The Mo/Al increase might also reflect increasing Atlantic water influx across the Gibraltar Sill, subsequent to the flooding event.

Oxygenation Mechanism and Modeling Results. A likely oxygen source to the eastern Mediterranean water column is the ~1.5-km-high cascade that refilled the eastern basin through the Noto Canyon southeast of Sicily (2, 14, 15). The canyon opens at the Malta Escarpment, with a 70° relief at its final 700 m drop to the Ionian Basin (14, 15). Modern experiments and observations demonstrate a high potential for cascading, with turbulent waters increasing the dissolved oxygen content, due to high aeration efficiency (43–46). Increasing flood discharge rates rapidly increase the dissolved oxygen content, commonly reaching supersaturated conditions exceeding 180 % O_2 further downstream (44). By comparison, mountain streams with an average ~30° slope have dissolved O_2 saturation of 90 to 120 % (46).

Numerical simulations of the MSC-terminating megaflood indicate that, at peak flood conditions, flood discharge may have exceeded 150 Sv, with velocities up to 50 m s^{-1} in the Alboran basin (2, 4). Remnant western basin Messinian liquids would have mixed completely with Atlantic waters due to the flood energy (thus, increasing mixing depth), eventually reaching the Sicily sill level (*SI Appendix*, Fig. S5). The cascade entering the eastern basin across the Sicily sill would have been even more energetic due to a steep drop at the Malta Escarpment, which would have generated highly turbulent conditions (2). It can, therefore, be expected that the eastern basin inflow was saturated (to supersaturated) in oxygen (*SI Appendix*, Fig. S5 and Fig. 3). In such a scenario, the eastern Mediterranean would have filled with highly saline (~80 PSU at flood termination, with starting Messinian fluids at gypsum saturation, ~140 PSU) and oxygenated waters up to the Sicily sill level (*SI Appendix*, Fig. S5) by the time the flooding phase was completed (within ~700 d) (2, 4). We hypothesize that the subsequent persistence of O_2 beneath the pycnocline would depend on the oxygen utilization rate by remineralization of the sinking organic carbon flux (hence, productivity). From our proxy evidence, we infer that O_2 may have been present for 8 to 12 thousand years following the flooding event, and that anoxic conditions were reached subsequently through the water column up to Sicily sill level (Fig. 3 and *SI Appendix*, Fig. S5 and *Materials and Methods*).

To test our hypothesis, we extend a published numerical model for post-MSC basin developments (2) to quantify oxygen concentrations during and after the flooding event (*Materials and Methods*). While a kilometer-scale drawdown is mandatory for catastrophic termination and oxygenation, the terminal MSC geochemical configuration of the Mediterranean remains debated, with suggestions of deep remnant brines or oligohaline conditions
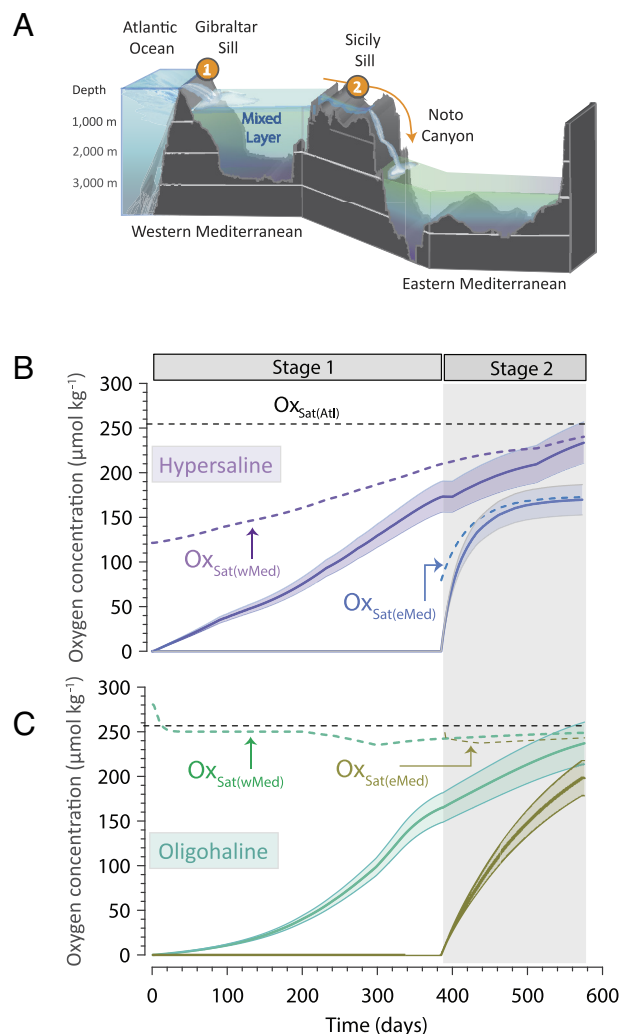

Fig. 3. Flooding phase and Mediterranean oxygenation. (*A*) Sketch of the eastern basin refilling phase by western basin waters flowing over the Sicily sill. Circled numbers 1 and 2 indicate ventilated inflows at the Gibraltar sill (Zanclean channel) and Sicily sill (Noto canyon). (*B*) Evolution of western (solid purple line) and eastern (solid blue line) basin mixed layer O_2 concentrations through the first two flood stages, for 100 % O_2 saturated inflows, for a largely hypersaline basin in the latest Messinian (*Materials and Methods*). (*C*) same as in (*B*), for a largely oligohaline latest Messinian basin. For (*B*) and (*C*), shaded lower and upper lobes for each curve represent the range of O_2 concentrations for 90 and 110 % O_2 saturated inflows entering each basin. Dashed lines represent O_2 saturation concentration for western ($Ox_{Sat(wMed)}$, purple) and eastern ($Ox_{Sat(eMed)}$, blue) basins. $Ox_{Sat(Atl)}$, Atlantic water oxygen saturation concentration.

before Atlantic reconnection. Moreover, the depths to which oligohaline or hypersaline conditions extended remain unknown. To include all possibilities, we consider two end-member scenarios, 1) a largely hypersaline basin with a thin surface low-salinity layer (200 PSU starting brine salinity) and 2) a largely oligohaline basin with only the deepest 3% of volume occupied by gypsum-saturated brines. We also explain why a 100% oligohaline basin cannot produce the observed eastern Mediterranean mystery sapropel deposition.

In the first model phase, we calculate the flow-energy-dependent extent of mixing of incoming western Mediterranean waters with eastern basin brines. This allows oxygen concentration calculation for western and eastern basin mixed layers through the refilling event, across a range of saturation states (Fig. 3 *B* and *C*). For the largely hypersaline setting, model results indicate that at 20 % mixing efficiency (*Materials and Methods*), ~95 % of eastern basin brines will mix completely with flood waters to create a hypersaline

layer with ~90 PSU below the Sicily sill, while residual brines remain in the deepest basin at flood termination (Fig. 4*A* and *SI Appendix*, Fig. S5). Assuming O_2-saturated inflow during refilling, the mixed layer reaches a 170 µmol kg^{-1} O_2 concentration, which is ~90 % of its O_2 saturation level (Fig. 3*B* and *Materials and Methods*). Our sensitivity tests indicate that, for a range of 80 to 175 % O_2 saturation of the inflow, the final eastern basin total O_2 content below Sicily sill depth can range between 2.8×10^{14} and 6.3×10^{14} mol (Fig. 4).
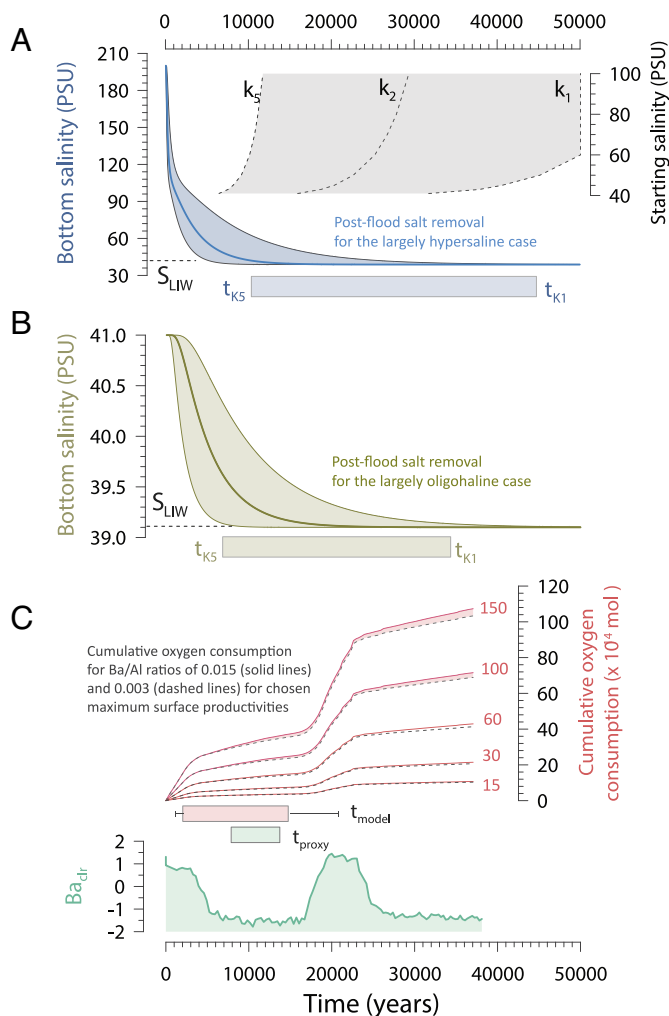
Fig. 4. Evolving phase, postflood eastern basin oxygen consumption. (*A*) Eastern basin postflood bottom salinity evolution for the largely hypersaline scenario, indicating an 11 to 44-thousand-year period to break the stratification via diapycnal diffusion. The light blue box indicates the time window of salt removal. The black dashed lines with gray shading show the time scales of salt removal for different starting salinities below Sicily Sill level (40-100 PSU range) following the flooding event. The k1, k2, and k5 curves correspond to salt removal time at 1×10^{-5}, 2×10^{-5}, and 5×10^{-5} m^2 s^{-1} turbulent diffusivities, respectively. For example, at a 2×10^{-5} m^2 s^{-1} turbulent diffusivity, salt removal to the Atlantic requires ~16,000 to 30,000 y for 40 and 100 PSU salinities, respectively. At 1×10^{-5} m^{2}s^{-1}, salt removal takes >50,000 y for salinities >60 PSU. (*B*) Same as in (*A*), for a largely oligohaline scenario. S_{LIW}, Levantine intermediate water salinity. (*C*) Cumulative oxygen consumption required to degrade all organic matter sinking below the Sicily sill level, at selected maximum sapropel surface productivity values (from 15 to 150 gC m^{-2} y^{-1}, as indicated by pink numbers on each curve). Solid and dashed lines correspond to higher and lower Ba/Al ranges chosen in calculations (*Materials and Methods*). Time initiates at the M/P boundary. The pink box (t_{model}) indicates the possible time range from the model (for an O_2 saturated inflow), after which O_2 below Sicily sill is consumed completely. Gray side bars indicate minimum (0.6 kyr) and maximum (20.5 kyr) oxygen persistence durations, at 80 % and 175 % inflow O_2 saturation. The green box (t_{proxy}) indicates the proxy-based estimated minimum and maximum durations for an oxygenated eastern Mediterranean (8 to 12 thousand year; see *Materials and Methods*).

For the largely oligohaline setting with thick brackish water columns in both subbasins (only 3% volume percentage of the deepest basin comprising gypsum-saturated brines), the western Mediterranean rapidly becomes fully mixed and oxygenated due to the higher density of sea water. Following transfer over the Sicily sill, the eastern basin becomes slightly more oxygenated (~200 µmol kg^{-1}) compared to the hypersaline scenario, due to the higher oxygen saturation capacity of low-salinity waters (Fig. 3*C*). At flood termination, the eastern basin becomes stratified at the Sicily sill level with waters of slightly enhanced salinity [~41 PSU, approximately 2.5 PSU above the normal eastern Mediterranean salinity (Fig. 4*B*)]. Overall, our two end member model scenarios indicate that, for both largely hypersaline and oligohaline preexisting conditions, the eastern basin will be stratified and oxygenated up to the Sicily sill at flood termination (Figs. 3 and 4 and *Materials and Methods*). However, a 100% oligohaline Mediterranean during the terminal MSC will not allow the observed geochemical signatures and the observed mystery sapropel deposition. In this case, eastern basin salinity at flood termination will be lower than Atlantic salinity, which will result in resumed deep-water renewal following the refilling event. Therefore, sapropel deposition and sedimentary Mo enrichment would not have occurred if the deep Mediterranean had been occupied entirely by oligohaline waters in the terminal MSC. The data are, therefore, inconsistent with that scenario.

Salt removal back to the Atlantic after flood termination was suggested to occur via turbulent diffusion (2). In our model, with a diapycnal diffusivity range of 1×10^{-5} to 5×10^{-5} m^2 s^{-1}, eastern basin deep water renewal was inhibited for 12,000 to >50,000 y in the largely hypersaline scenario following flooding (*SI Appendix*, Fig. S6). For the largely oligohaline stratified eastern basin scenario with low-salinity contrast with surface waters, salt diffusion may require >37,000 y at a 1×10^{-5} m^2 s^{-1} turbulent diffusivity, for salinities greater than 43 PSU (*SI Appendix*, Fig. S6). Our sensitivity tests suggest that for a range of stratification strengths between 40 and 100 PSU below Sicily sill level, salt diffusion time scales back to the Atlantic can range between 6,000 and >50,000 y (*SI Appendix*, Fig. S6). Our revised proxy-based age estimate for the mystery sapropel (33,000 y; see above) is consistent with this suggested stratification duration for largely oligohaline to hypersaline scenarios (*SI Appendix*, Fig. S6). To estimate the postflood O_2 consumption rate, the second phase of our model employs a modified algorithm that links the sedimentary Ba accumulation rate to surface-water productivity, which is further evaluated with statistical testing (47, 48) (*Materials and Methods* and *SI Appendix*, Figs. S7 and S8). We estimate absolute organic carbon fluxes through time for a range of maximum sapropel productivity values (15 to 150 gC m^{-2} y^{-1}) (48–50). We find that, for a basin refilled with O_2 saturated inflow under the largely hypersaline scenario, complete O_2 consumption may take 0.4 to 13.5 thousand years within the 15 to 150 gC m^{-2} y^{-1} surface productivity range (Fig. 4*C*). With higher oxygen availability in the oligohaline scenario, the maximum duration extends to 17 thousand years (Fig. 4 and *SI Appendix*, Fig. S6). We note that this range covers the average surface productivity range of 30 to 60 gC m^{-2} y^{-1} during Quaternary sapropel formation, the 120 to 140 gC m^{-2} y^{-1} range of Late Pliocene sapropels (49, 50), and the 5 to 7 times lower values for sapropels formed before 3.2 Ma (from Ba accumulation rate changes (25); *SI Appendix*, Fig. S9). Our sensitivity tests indicate that following a refilling event with saturated to supersaturated flood waters, and for maximum sapropel productivities lower than ~45 gC m^{-2} y^{-1}, it is possible to maintain oxic to suboxic eastern Mediterranean conditions for the observed 8 to 12-thousand-year period (Fig. 4 and *SI Appendix*, Fig. S6).

Discussion

Our model simulations involve a few key assumptions, and we have carried out sensitivity tests to account for associated uncertainties (*Materials and Methods* and Figs. 3 and 4). In the first model phase (Mediterranean refilling), we employed constant Noto Canyon dimensions throughout the eastern basin's refilling phase. In reality, the Malta Escarpment may have been carved by the energetic flow across the Sicily sill, gradually expanding the Noto Canyon to its present-day dimensions (14, 51). A smaller canyon would have allowed an even more energetic flow to the eastern basin, entirely mixing eastern basin Messinian liquids with flood waters more rapidly than the model results suggest. However, this assumption does not affect our results because the final oxygen content would be the same irrespective of canyon dimensions. The surface productivity estimate employed for the second model phase (postflood oxygen consumption rate estimation) is constrained to a constant value for the whole eastern Mediterranean, due to a lack of sediment records extending through the mystery sapropel across the M/P boundary. Paleoproductivity estimates suggest that total export production during sapropel deposition may have been slightly higher in western parts of the eastern Mediterranean (49). Our sensitivity tests account for this uncertainty by including a range of surface productivity estimates that cover the spectrum of eastern Mediterranean productivity estimates (Fig. 4 and *SI Appendix*, Fig. S6).

While the Mediterranean terminal Messinian hydrogeochemical configuration is debated, our proxy data and model simulations suggest a substantially lower Mediterranean base level immediately before Atlantic reconnection at 5.33 Myr. This low base level would have allowed an increasingly energetic Atlantic flow to the Mediterranean, refilling the entire basin within 2 y (Fig. 3 and *SI Appendix*, Fig. S5). Our findings improve upon previously reported land-to-sea indicators of a megaflood, including implications for a rapid refilling event suggested from contouritic deposits in Sicily (16), western Mediterranean erosional features, and chaotic sedimentary deposits detected at the base of the Malta Escarpment that have been related to flood-related western basin erosion (14, 15, 51). Moreover, we provide water column indicators of flood-driven oxygenation, further supporting the aforementioned sedimentary and seismic evidence for the Zanclean megaflood.

In summary, we employ wide-ranging data and box models to explore the transitional phase to normal marine conditions following the catastrophic marine flooding that terminated the 600,000-y Messinian Mediterranean isolation from the global ocean (2, 4). Our analysis suggests that, despite arguments for dominantly hypersaline or oligohaline conditions in the terminal Messinian, the eastern basin will be salinity-stratified at the end of a catastrophic refilling phase. Unlike normal sapropels, the "mystery sapropel" reflects organic matter deposition under a largely oxygenated eastern Mediterranean water column, which resulted from aeration by the violent flooding event. The eastern Mediterranean then changed gradually from an oxidizing to a reducing state over ~8 to 12,000 y due to organic matter respiration, while stratification was weakened over ~33,000 y. These results provide the first independent evidence of the consequences of the post-Messinian megaflood on Mediterranean basin evolution.

Materials and Methods

X-Ray Fluorescence Scanning. We present X-ray fluorescence core-scanning (XRF-CS) data for ODP Site 969 Hole B (95.9–98.3 mbsf). Archive core sections were scanned at MARUM-University of Bremen on an Avaatech XRF core scanner. Core sections were covered with 4-mm-thick Ultralene film and measured at 50

and 30 kV with 0.55 mA current and with Cu and Pd-thick filters, respectively, and at 10 kV with 0.035 mA current (no filter); count time for all runs was 7 s. XRF-CS element intensities are presented as logarithmic ratios between elements for Ba/Al and Mo/Al. Moreover, individual elements (Ca and S) are plotted after centered log-ratio transformation (clr) following ref. 52.

Biostratigraphy. To identify the M/P boundary, previous studies of the mystery sapropel employed shipboard stratigraphy and biostratigraphy based on post-cruise scientific reports of ODP site 969. To generate a preliminary chronology for Site 969, we tuned Ba (and Ba/Al) peaks to June 21st 65°N insolation maxima (53), assuming that the M/P boundary occurs at 97.11 m in the core. To validate our XRF-based chronology, Site 969 biostratigraphy was reevaluated.

The Zanclean global stratotype section and point (GSSP) and the base of the Pliocene is defined at the base of carbonate cycle 1 in the Eraclea Minoa section, Sicily (54). Therefore, to determine whether the inferred M/P boundary is placed correctly at Site 969 and whether the basal Pliocene section at Site 969 is complete, comparison with the Eraclea Minoa section is required. To detect earliest Pliocene biozones, comparison of *Sphaeroidinellopsis* and left coiled neogloboquadrina species was carried out using 17 samples from core sections A11H4, A11H5, B11H5, and B11H6. Long-distance comparisons of these bioevents have been incorporated in several Mediterranean M/P transition studies (8, 29, 55). To confirm the M/P boundary position, comparison of Site 969 sapropels between Eraclea Minoa gray intervals was employed (*SI Appendix*, Fig. S2).

Previous studies have suggested that the oldest sapropel-marl succession (corresponding to cycle 1 at the Eraclea Minoa section) is likely absent at ODP Site 969. Cycle 1 spans from 5,332 kyr to 5,310 kyr. However, identification of *R. zancleana* and *Crocodylus acutus* (5,332 kyr) in later studies (*SI Appendix*, Table S1), and the presence of the first *Neogloboquadrina acostaensis* sinistral shift (5,321 kyr), suggest that cycle 1 is also recorded at Site 969. Based on linear sedimentation rate estimates with bioevents for the earliest Pliocene sediments, cycle 1 is likely complete at Site 969 (*SI Appendix*, Fig. S2).

X-Ray Diffraction Analysis. A total of 10 and 8 samples were chosen from ODP 967 and 969 sediments, respectively, across the M/P boundary. Each sample was ground by hand in acetone with an agate mortar and dried. To enable amorphous material quantification, samples were spiked with 20 wt% corundum (Al_2O_3, 1 µm, Baikalox®), mixed in acetone, pipetted onto a quartz low-background-holder, and dried. Powder XRD analysis was carried out with a Malvern Panalytical Empyrean Series 3 which is equipped with Bragg–Brentano HD divergent beam optics and a PIXcel3D detector (1D scanning mode, 3.347° active length), using CoKα radiation. The sample was analyzed over a range of 4 to 85° 2θ, with step width of 0.0262606° 2θ and a total dwell time of 300 s/step, while spinning horizontally. Phase identification was carried out with the DiffracPlus Eva 10 software (2004) and ICDD PDF-2 database (2004). Siroquant V4 (2014) was used for phase quantification.

Organic Carbon Quantification. To determine organic carbon percentages across the M/P boundary, 10 samples from Site 967 and 11 samples from Site 969 were chosen. All samples were analyzed at the Environmental Analysis Lab (EAL), Southern Cross University. Approximately 0.2 g of dry, powdered sample was weighed into nickel-lined ceramic LECO boats. An excess (approx. 2 ml) of 5% sulfurous acid was added to each sediment sample and reference sample. Then, samples were placed on a hotplate at ~100 °C to dry. Analyses were carried out with a LECO SC832 following the QWORK18-70 and LECO SC832 Operation Manual, with automatic carbon content measurements.

Biomarker Analysis. For biomarker analysis, ~2 g per sample was sampled from cores from ODP Site 969. The samples were dried and finely ground using a mortar and pestle. Powdered sediments were extracted with a Dionex Accelerated Solvent Extractor (ASE 200) using 90 % dichloromethane and 10 % methanol. Each cell was heated to 100 °C (2 min), pressurized to 1000 psi (5 min thermal equilibration), static extracted (2 min), flushed, and purged of solvent residue using pressurized nitrogen for five cycles.

Preparation of the total lipid neutral (TLN) extract for gas chromatography–mass spectrometry (GC–MS) analysis. The total lipid extract (TLE) was evaporated to dryness under N_2 gas at 45 °C (Caliper TurboVap LV) and hydrolyzed overnight with 3 mL of 6 % KOH in methanol:water = 8:2. The solution was flushed with N_2, vortexed, and left overnight at room temperature. TLNs were obtained after three backextractions with *n*-hexane (3 mL) and washing with MilliQ water (1

mL) to remove any remaining KOH. Solvent was removed from the TLN under a purified N_2 stream at 60 °C. Aqueous layers were combined for FA extraction.

The TLN was taken up in dichloromethane and transferred to a 2 mL vial including a 100 μL insert and then reduced to dryness. BSTFA (sigma) (50 μL) was added to derivatize the TLN, and the solution was heated at 80 °C overnight. Excess BSTFA was removed as above with a purified N_2 gas stream. Hexane was added to the TLN for immediate GC–MS analysis.

FA extract preparation for GC–MS analysis. Combined aqueous phases from the TLN extraction were acidified to pH 1 with HCl (32%). The FA fraction was extracted from the acidified solution using dichloromethane and treated as above to derivatize with BSTFA.

Gas chromatography and mass spectrometry. GC–MS analyses were carried out on an Agilent 6890 GC coupled to a Micromass Autospec Premier double-sector MS (Waters Corporation, Milford, MA). The GC is equipped with a 60 m DB-5MS capillary column (0.25 mm internal diameter, 0.25 μm film thickness; Agilent) and used helium as the carrier gas at a constant flow rate of 1 mL min^{-1}. The MS source was operated at 260 °C in EI-mode at 70 eV ionization energy and with 8,000 V accelerating voltage. Samples were injected in splitless mode into a Gerstel PTV injector, which was ramped from 60 °C (hold for 0.1 min) to 300 °C at 260 °C/min and held at the maximum temperature for the remaining analysis duration. For full-scan analyses, the GC oven was held at 60 °C for 4 min, heated to 315 °C at 4 °C/min, with a final hold time of 22.3 min. The AutoSpec full-scan duration was 0.7 s plus 0.2 s interscan delay over a 55 to 600 Da mass range.

All samples were injected in n-hexane to avoid chromatographic signal deterioration by $FeCl_2$ build-up in the MS ion source through use of halogenated solvents. All components were quantified relative to the 18-MEAME internal standard (m/z 340), using characteristic parent-to-daughter ion mass transitions (m/z in brackets, n-alkanes (85), n-alkanols (75), dinosterol (69), C30 diol (69), friedelin (205), gammacerane (191), tetrahymanol (191), archaeol (85), respectively). Peak areas are uncorrected for GC–MS response differences. All data required for calculation of indicated ratios in the main text are in *SI Appendix*, Table S3.

Pollen and Microcharcoal Analysis. To determine pollen and microcharcoal concentrations, ~1.25 cm^3 of sediment was dispersed in Calgon (3%) and placed in a low-temperature water bath for ½ h and then on an agitator overnight to further loosen the sediment; a *Lycopodium* tablet was added (9666 spores) to enable pollen and charcoal concentration calculation. Samples were then treated with HCl (10%) in a warm bath to remove carbonates and were then sieved at >125 μm; the >125 μm fraction provided no relevant material (plant or seed material). A heavy liquid (lithium heteropolytungstate) with 2.01 density (specific gravity) was then used to separate mineral matter from the organic fraction, followed by acetolysis which removes cellulose and stains the pollen. Samples were then mounted on slides with glycerin; the cover slip was sealed with nail polish. Glycerin aids identification and provides movability on the slide. Distilled H_2O washes, repeated two to three times, were completed for all steps.

Mediterranean Evolution.
Flooding phase oxygen concentration. Following recent studies on the post-Messinian megaflood, we assume water level drops of 2,000 m and 1,750 m for eastern and western basins, respectively, before the flood (2). To allow all possible Mediterranean geochemical configurations, we separately considered, 1) largely hypersaline conditions and 2) largely oligohaline conditions before Atlantic reconnection. For the largely hypersaline scenario, we updated initial eastern basin Messinian brine salinity to 200 PSU to generate a residual brine layer at flood termination (choice validated by ref. 2, because all western basin brines will be transferred to the eastern basin below 220 PSU). A brackish water (20 PSU) layer of 100 m thickness was included above the brines for this scenario. In the largely oligohaline case, only 3% by volume of the deepest parts of each basin was filled with gypsum-saturated brines (140 PSU), while the rest of the deep basins were filled entirely with brackish waters. Flood velocity, energy, and western and eastern basin salinity evolution for both scenarios are calculated according to published methods, using the most recent Mediterranean hypsometry (2, 4). We use a 20 % mixing efficiency during flooding (for mixing of less-saline waters with dense brines) because proxy data agree well with this value (2).

During the first flooding stage, the western Mediterranean was refilled rapidly by Atlantic waters. Modern observations indicate that turbulent rapids and falling water rapidly become oxygen saturated, commonly reaching supersaturated levels up to

180 % further downstream (43–45). Due to the high flow energy and turbulence, we assume that oxygen-saturated normal marine flood waters (36 PSU salinity, 15 °C temperature) enter the western basin. To calculate the Atlantic inflow saturated oxygen concentration ($Ox_{Atlantic}$), we incorporate the Gibbs Sea Water (GSW) Oceanographic Toolbox in our model. The GSW toolbox function *O2sol* calculates the saturated oxygen concentration, depending on floodwater salinity and temperature.

The mixing extent of Atlantic waters with western basin fluids (hypersaline or oligohaline) depends on available flow kinetic energy reaching the basin surface. If the flow energy exceeds the potential energy gain required for complete mixing, the entire water column will mix with incoming Atlantic waters. If the flow energy is insufficient to mix with western basin water completely, a portion of the brine column will be mixed, creating a "mixed layer". Following ref. 2, we compute the mixing extent using

$$KE_{Av} = PE_{GP}$$
$$= \int_{H+h-H_{Mix}}^{H+h} \rho_m gzdzA(z) - \left(\int_H^{H+h} \rho_s gzdzA(z) + \int_{H+h-H_{Mix}}^{H} \rho_b gzdzA(z) \right),$$
[1]

where KE_{Av} is the flow kinetic energy available for mixing, PE_{GP} is the potential energy gain during partial mixing, H is the total water column thickness before mixing, h is the seawater layer thickness that floods into the basin per timestep (per day), H_{Mix} is the mixed layer thickness, g is the acceleration due to gravity, $A(z)$ is the basin surface area with depth (z), and ρ_m, ρ_s, and ρ_b are densities of the mixed layer, Atlantic waters, and Messinian brines/brackish waters, respectively.

Mixed layer thickness (H_{Mix}) can then be used to calculate the mixed layer volume ($V_{Mix[wMed]}$). Therefore, the western basin mixed layer oxygen concentration at each timestep will be

$$Ox_{wMed} = \frac{Ox_{Atlantic} \times Q_{in}}{V_{Mix[wMed]}}.$$
[2]

During flood stage 2, the eastern basin is filled by western basin mixed layer waters through Noto Canyon (2). Thus, the eastern basin inflow oxygen concentration (Ox_{Noto}) is determined by the properties (salinity, temperature) of the western basin mixed layer. Eastern basin mixed layer thickness and volume are calculated using Eq. **1**. Therefore, the eastern basin mixed layer oxygen concentration at each timestep will be

$$Ox_{eMed} = \frac{Ox_{Noto} \times Q_{in}}{V_{Mix[eMed]}}.$$
[3]

Once the eastern basin reaches the Sicily sill level, the Noto Canyon cascade terminates. During final stage flooding, both western and eastern basin levels rise to the Atlantic level. The eastern basin becomes salinity-stratified at the Sicily sill level, while the western basin becomes a normal marine basin. We assume that oxygen contents in the western basin, and in the eastern basin below the Sicily sill level, remained constant due to diminished flow energy during final flooding (2).
Sensitivity Test 1. Flooding phase evolution for a completely desiccated western basin.

To test whether brine transfer from the western basin is required for eastern basin stratification, we run our model simulation for a completely desiccated western Mediterranean. Our results indicate that, even without brine transfer, the eastern Mediterranean will be salinity-stratified at the Sicily Sill with a 66 PSU salinity below sill level.

Postflood Eastern Mediterranean Oxygen Consumption. Our flooding model indicates that the eastern basin is mixed to a ~3,300 m depth due to the flood energy (at 20% mixing efficiency as in ref. 2) and that oxygen concentrations within the mixed layer can reach up to 170 μmol kg^{-1} for the hypersaline scenario (200 μmol kg^{-1} for the oligohaline scenario). As density stratification prevents deep water formation, oxygen consumption will occur due to sinking organic matter. Our proxy data suggest a period of 8 to 12 thousand years to consume all oxygen by sinking organic matter (based on biomarker data and peak S contents and rising Mo contents at ~5,325 kyr and subsequently increasing pyrite contents back to Messinian levels at 5,321 kyr).

To estimate oxygen consumption rates with time, we calculate the relative eastern basin barium flux. Marine barite ($BaSO_4$) is a major water-column particulate Ba carrier and is precipitated during phytoplankton decay, which produces

a positive correlation between biogenic barium and organic carbon flux to the seafloor (47, 48). Algorithms developed on this relationship are used to estimate past ocean basin productivity, including for the Mediterranean (47, 48).

The goal of organic carbon flux calculation is to obtain a range of possible productivity values through the mystery sapropel period for the entire eastern Mediterranean. Ba flux calculations across sapropel–marl cycles for different eastern Mediterranean sites indicate that the export productivity pattern remains largely the same over the eastern Mediterranean (56). Therefore, we scale the Mediterranean Ridge productivity value to different maximum productivity curves applicable to different eastern basin regions. To estimate the biogenic Ba flux, the terrigenous Ba component should be removed, usually using conservative element concentrations such as Al. Therefore, the biogenic Ba flux can be written as

$$Ba_{bio} = Ba_{total} - \left(Al \times \frac{Ba}{Al_{aluminosilicate}} \right), \quad [4]$$

where Ba_{bio} is the biogenic Ba content, Ba_{total} is the total Ba content, and $Ba/Al_{aluminosilicate}$ is the terrigenous Ba/Al ratio, which is considered here to be 0.0019 for the eastern Mediterranean (49). To scale the Al content in Eq. **5** with respect to Ba, we use a range of Ba/Al values for the Early Pliocene for both sapropel and marl intervals (*SI Appendix*, Fig. S9). Our calculations indicate that the biogenic Ba flux does not have a major impact on oxygen consumption time scales. Then, the Ba_{bio} flux (F_{Ba}) can be estimated using

$$F_{Ba} = \frac{Ba_{bio} \times \frac{MAR}{100}}{0.209 \log(MAR) - 0.213}, \quad [5]$$

where MAR is the mass accumulation rate. New production (P_{new}) can then be estimated using

$$P_{new} = \left(\frac{F_{Ba} \times 0.171 \times Ba_{dis}^{2.218} \times z^{(0.476 - 0.00478 Ba_{dis})}}{2056} \right)^{1.504}, \quad [6]$$

where Ba_{dis} is the mean Mediterranean dissolved Ba concentration and z is the water depth at the deposition site. Surface primary productivity (PP) is then given by

$$PP = 20 \left(P_{new} \right)^{0.5}. \quad [7]$$

With the above parameterizations, we can estimate eastern Mediterranean export productivity. We, thus, use uncalibrated ODP Site 969 XRF-CS data for export productivity reconstruction, scaled using a relative productivity curve. Subsequently, these values were converted to absolute productivity curves that are applicable to the entire Mediterranean.

Mediterranean paleoproductivity estimates indicate that surface primary productivity during peak sapropel intervals generally ranged between 30 and 60 gC m^{-2} y^{-1}, with extreme values of 15 gC m^{-2} y^{-1} and exceeding 120 gC m^{-2} y^{-1} recorded (49, 50). To generate a relative productivity curve, we assume that the maximum absolute surface productivity was reached at the point of maximum Ba flux following the M/P boundary. Eqs. **5**–**7** are then used to calculate relative PP values. Assuming a constant sedimentation rate through the mystery sapropel, we use a ratio of 1.3 for $MAR_{marl}/MAR_{sapropel}$ during precession maxima for Eq. **5**. If PP_{Array} contains all PP values calculated using Ba and Al counts, then the relative productivity curve $PP_{R(Array)}$ will be

$$PP_{R(Array)} = \frac{PP_{(Array)}}{PP_{(Array)}^{max}}, \quad [8]$$

where $PP_{(Array)}^{max}$ is the maximum value in $PP_{(Array)}$, which occurs at maximum F_{Ba}. Therefore, the maximum $PP_{R(Array)}$ value also occurs at maximum F_{Ba} ($PP_{R(Array)}^{max} = 1$). Then, the absolute productivity curve ($PP_{abs(Array)}$) can be estimated using

$$PP_{abs(Array)} = PP_{R(Array)} \times PP_{abs}^{max}, \quad [9]$$

where PP_{abs}^{max} is the chosen maximum absolute productivity value. We estimate absolute surface productivity curves at chosen PP_{abs}^{max} values ranging between 15 and 150 gC m^{-2} y^{-1}.

In modern settings (including the Mediterranean), a maximum of ~25 % of surface primary production leaves the photic zone. A further 60 to 80 % of organic carbon export below the photic zone is oxidized within the next several hundred meters (57, 58). We use these values to estimate organic carbon export with time, below Sicily sill level (present depth = 430 m). Therefore, total organic carbon export to the deep basin ($C_{exp(deep)}$) through time can be estimated using

$$C_{exp(deep)} = PP_{abs(Array)} \times 0.25 \times 0.3 \times A_{Sicily}, \quad [10]$$

where A_{Sicily} is the Mediterranean area at the Sicily sill level. A molar ratio of 1:1.4 for organic carbon: Oxygen is employed to calculate cumulative oxygen consumption below the stratification. Upward turbulent oxygen diffusion is much slower than the organic carbon sinking rate, so the average oxygen consumption rate (R_{ox}) below the Sicily sill is

$$R_{ox} = \frac{C_{exp(deep)} \times 1.4}{12}, \quad [11]$$

where the denominator is the molar mass of C in g mol^{-1}.

Ba_{bio}, Ba_{dis}, and z in Eqs. **5** and **6** are constants, so initial use of a relative productivity curve does not affect the result. To represent the range of potential values, we used a range of maximum productivity values as mentioned in Eq. **8**. To evaluate our results, we employ a Monte Carlo-style approach to introduce a broad range of maximum surface productivity values for the eastern Mediterranean (*SI Appendix*, Fig. S8). We evaluate our simulation for 250 random surface productivity values between 15 and 150 gC m^{-2} y^{-1}. This test gives us a range of values for deep-basin organic carbon export and oxygen consumption through time, and reproduces the individual curves obtained using selected PP_{abs}^{max} values in Eq. **10**. Our additional test further proves that for maximum productivity values of 45 gC m^{-2} y^{-1} or lower, a 12,000 y or greater oxygen consumption phase can be maintained in the deep eastern Mediterranean.

Data, Materials, and Software Availability. All other data are included in the manuscript and/or supporting information. Previously published data were used for this work (2, 25).

Author affiliations: ^{a}Department of Geosciences, Princeton University, Princeton, NJ 08544; ^{b}Research School of Earth Sciences, Australian National University, Canberra, ACT 0200, Australia; ^{c}Department of Earth Sciences, University of Utrecht, Utrecht 3584 CD, The Netherlands; ^{d}Department of Ocean Systems, Royal Netherlands Institute for Sea Research (Nederlands Instituut voor Onderzoek der Zee), Den Burg 1790 AB, Texel, The Netherlands; ^{e}Center for Marine Environmental Sciences, University of Bremen, Bremen D-28359, Germany; ^{f}School of Culture, History and Language, College of Asia and the Pacific, Australian National University, Canberra, ACT 2601, Australia; ^{g}Research School of Physics, Australian National University, Canberra, ACT 2601, Australia; ^{h}Australian Research Council Centre of Excellence for Australian Biodiversity and Heritage, School of Culture, History and Language, Australian National University, Canberra, ACT 2601, Australia; ^{i}Geosciences Barcelona, Consejo Superior de Investigaciones Científicas, Barcelona 08028, Spain; ^{j}Australian Research Council Centre of Excellence for Climate Extremes, Australian National University, Canberra, ACT, Australia; and ^{k}Ocean and Earth Science, University of Southampton, National Oceanography Centre, Southampton SO14 3ZH, United Kingdom

Author contributions: U.A. and J.J.B. designed research; U.A., J.M.H., W.-J.Z., R.H., I.v.d.H., S.R., and U.T. performed research; J.J.B., U.R., and S.H. contributed new reagents/analytic tools; U.A., J.M.H., and U.T. analyzed data; J.J.B., P.T.M., W.-J.Z., A.S., W.K., D.G.-C., G.-J.R., and A.P.R. reviewed and edited the paper; K.M.G., A.M.H., A.P.R., and E.J.R. supervised the study; and U.A., J.J.B., W.-J.Z., A.P.R., and E.J.R. wrote the paper.

1. W. Krijgsman *et al.*, Causes and consequences of the Messinian salinity crisis. *Nat. Rev. Earth Environ.* **5**, 335–350 (2024).
2. U. Amarathunga *et al.*, Sill-controlled salinity contrasts followed post-Messinian flooding of the Mediterranean. *Nat. Geosci.* **15**, 720–725 (2022).
3. W. Krijgsman, F. J. Hilgen, I. Raffi, F. J. Sierro, D. S. Wilson, Chronology, causes and progression of the Messinian salinity crisis. *Nature* **400**, 652–655 (1999).
4. D. Garcia-Castellanos *et al.*, Catastrophic flood of the Mediterranean after the Messinian salinity crisis. *Nature* **462**, 778–781 (2009).

5. K. J. Hsü, W. B. F. Ryan, M. B. Cita, Late miocene desiccation of the Mediterranean. *Nature* **242**, 240–244 (1973).

6. G. Clauzon, J.-P. Suc, F. Gautier, A. Berger, M.-F. Loutre, Alternate interpretation of the Messinian salinity crisis: Controversy resolved?. *Geol* **24**, 363 (1996).

7. P. M. Barber, Messinian subaerial erosion of the proto-Nile Delta. *Mar. Geol.* **44**, 253–272 (1981).

8. A. Caruso, M.-M. Blanc-Valleron, S. Prato, C. Pierre, J. M. Rouchy, The late messinian "lago-mare" event and the Zanclean reflooding in the Mediterranean sea: New insights from the cuevas del almanzora section (Vera Basin, South-Eastern Spain). *Earth-Sci. Rev.* **200**, 102993 (2020).

9. F. Andreetto et al., Freshening of the mediterranean salt giant: Controversies and certainties around the terminal (Upper Gypsum and Lago-Mare) phases of the Messinian Salinity Crisis. *Earth-Sci. Rev.* **216**, 103577 (2021).

10. J. García-Veigas, D. I. Cendón, L. Gibert, T. K. Lowenstein, D. Artiaga, Geochemical indicators in Western Mediterranean Messinian evaporites: Implications for the salinity crisis. *Mar. Geol.* **403**, 197–214 (2018).

11. F. Andreetto et al., High-amplitude water-level fluctuations at the end of the Mediterranean Messinian Salinity Crisis: Implications for gypsum formation, connectivity and global climate. *Earth Planet. Sci. Lett.* **595**, 117767 (2022).

12. A. Marzocchi, R. Flecker, C. G. C. van Baak, D. J. Lunt, W. Krijgsman, Mediterranean outflow pump: An alternative mechanism for the Lago-mare and the end of the Messinian Salinity Crisis. *Geology* **44**, 523–526 (2016).

13. F. Pilade et al., Deciphering the termination of the Messinian salinity crisis: The alkenone record of the Miocene-Pliocene transition in the northern Mediterranean. *Palaeogeogr. Palaeoclimatol. Palaeoecol.* **631**, 111831 (2023).

14. A. Micallef et al., Evidence of the Zanclean megaflood in the eastern Mediterranean Basin. *Sci. Rep.* **8**, 1078 (2018).

15. D. Garcia-Castellanos et al., The zanclean megaflood of the Mediterranean – Searching for independent evidence. *Earth-Sci. Rev.* **201**, 103061 (2020).

16. G. Dijk et al., A terminal Messinian flooding of the Mediterranean evidenced by contouritic deposits on Sicily. *Sedimentology* **70**, 1195–1223 (2023).

17. G. Aloisi, Chlorine isotopes constrain a major drawdown of the Mediterranean Sea during the Messinian Salinity Crisis. *Nat. Commun.* **15**, 9671 (2024).

18. M. Roveri et al., The messinian salinity crisis: Past and future of a great challenge for marine sciences. *Mar. Geol.* **352**, 25–58 (2014).

19. M. Rossignol-Strick, African monsoons, an immediate climate response to orbital insolation. *Nature* **304**, 46–49 (1983).

20. E. J. Rohling, G. Marino, K. M. Grant, Mediterranean climate and oceanography, and the periodic development of anoxic events (sapropels). *Earth-Sci. Rev.* **143**, 62–97 (2015).

21. D. Heslop, U. Amarathunga, E. J. Rohling, Estimating plio-Pleistocene North African monsoon runoff into the Mediterranean Sea and temperature impacts. *Paleoceanog and Paleoclimatol* **38**, e2023PA004677 (2023).

22. J. C. Larrasoaña, A. P. Roberts, A. Hayes, R. Wehausen, E. J. Rohling, Detecting missing beats in the Mediterranean climate rhythm from magnetic identification of oxidized sapropels (Ocean Drilling Program Leg 160). *Phys. Earth Planet. Inter.* **156**, 283–293 (2006).

23. G. J. De Lange et al., Synchronous basin-wide formation and redox-controlled preservation of a Mediterranean sapropel. *Nat. Geosci.* **1**, 606–610 (2008).

24. P. J. M. van Santvoort, G. J. de Lange, C. G. Langereis, M. J. Dekkers, M. Paterne, Geochemical and paleomagnetic evidence for the occurrence of "missing" sapropels in eastern Mediterranean sediments. *Paleoceanography* **12**, 773–786 (1997).

25. K. M. Grant et al., Organic carbon burial in Mediterranean sapropels intensified during Green Sahara periods since 3.2 Myr ago. *Commun. Earth Environ.* **3**, 11 (2022).

26. U. Amarathunga et al., Mid-Pliocene glaciation preceded by a 0.5-million-year North African humid period. *Nat. Geosci.* **17**, 660–666 (2024).

27. K. C. Robertson, C. Richter, *Shipboard Scientific Party. Site 969* (Data Publisher for Earth & Environmental Science, 1996).

28. A. Murat, H. Got, Organic carbon variations of the eastern Mediterranean Holocene sapropel: A key for understanding formation processes. *Palaeogeogr. Palaeoclimatol. Palaeoecol.* **158**, 241–257 (2000).

29. S. M. Iaccarino et al., The miocene-pliocene boundary and the significance of the earliest pliocene flooding in the Mediterranean Sea. *Mem. Soc. Geol. Ital.* **54**, 109–131 (1999).

30. C. Corselli, F. Aghib, Brine formation and gypsum precipitation in the Bannock Basin. *Mar. Geol.* **75**, 185–199 (1987).

31. J. Zhao et al., Non-evaporitic gypsum formed in marine sediments due to sulfate-methane transition zone fluctuations and mass transport deposits in the northern South China Sea. *Mar. Chem.* **233**, 103988 (2021).

32. H. F. Passier, J. J. Middelburg, G. J. De Lange, M. E. Böttcher, Pyrite contents, microtextures, and sulfur isotopes in relation to formation of the youngest eastern Mediterranean sapropel. *Geology* **25**, 519–522 (1997).

33. A. Filippidi, G. J. De Lange, Eastern Mediterranean deep water formation during Sapropel S1: A reconstruction using geochemical records along a bathymetric transect in the Adriatic outflow region. *Paleoceanogr. Paleoclimatol.* **34**, 409–429 (2019).

34. M. Natalicchio et al., An archaeal biomarker record of paleoenvironmental change across the onset of the Messinian salinity crisis in the absence of evaporites (Piedmont Basin, Italy). *Org. Geochem.* **113**, 242–253 (2017).

35. S. G. Wakeham, C. M. Lewis, E. C. Hopmans, S. Schouten, J. S. Sinninghe Damsté, Archaea mediate anaerobic oxidation of methane in deep euxinic waters of the Black Sea. *Geochim. Cosmochim. Acta* **67**, 1359–1374 (2003).

36. D. Menzel, P. F. van Bergen, S. Schouten, J. S. Sinninghe Damsté, Reconstruction of changes in export productivity during Pliocene sapropel deposition: A biomarker approach. *Palaeogeogr. Palaeoclimatol. Palaeoecol.* **190**, 273–287 (2003).

37. M. J. L. Hoefs, W. I. C. Rijpstra, J. S. Sinninghe Damsté, The influence of oxic degradation on the sedimentary biomarker record I: evidence from Madeira Abyssal Plain turbidites. *Geochimica et Cosmochimica Acta* **66**, 2719–2735 (2002).

38. K. A. Bogus et al., The effect of meter-scale lateral oxygen gradients at the sediment-water interface on selected organic matter based alteration, productivity and temperature proxies. *Biogeosciences* **9**, 1553–1570 (2012).

39. R. G. Keil, F. S. Hu, E. C. Tsamakis, J. I. Hedges, Pollen in marine sediments as an indicator of oxidation of organic matter. *Nature* **369**, 639–641 (1994).

40. J. Volkman, Sterols in microorganisms. *Appl. Microbiol. Biotechnol.* **60**, 495–506 (2003).

41. C. Scott, T. W. Lyons, Contrasting molybdenum cycling and isotopic properties in euxinic versus non-euxinic sediments and sedimentary rocks: Refining the paleoproxies. *Chem. Geol.* **324–325**, 19–27 (2012).

42. S. R. Emerson, S. S. Huested, Ocean anoxia and the concentrations of molybdenum and vanadium in seawater. *Mar. Chem.* **34**, 177–196 (1991).

43. A. J. Ulseth et al., Distinct air–water gas exchange regimes in low- and high-energy streams. *Nat. Geosci.* **12**, 259–263 (2019).

44. L. Li, C. Qin, Q. Peng, Z. Yan, Q. Gao, Numerical simulation of dissolved oxygen supersaturation flow over the Three Gorges Dam spillway. *Tinshhua Sci. Technol.* **15**, 574–579 (2010).

45. J. Lu et al., Dissolved oxygen transfer along falling water jets with developing surface disturbance. *J. Hydro-environ. Res.* **38**, 129–136 (2021).

46. M. B. Canadell, L. Gómez-Gener, M. Clémençon, S. N. Lane, T. J. Battin, Daily entropy of dissolved oxygen reveals different energetic regimes and drivers among high-mountain stream types. *Limnol. Oceanogr.* **66**, 1594–1610 (2021).

47. J. Dymond, E. Suess, M. Lyle, Barium in deep-sea sediment: A geochemical proxy for paleoproductivity. *Paleoceanography* **7**, 163–181 (1992).

48. K. Pfeifer, S. Kasten, C. Hensen, H. D. Schulz, Reconstruction of primary productivity from the barium contents in surface sediments of the South Atlantic Ocean. *Mar. Geol.* **177**, 13–24 (2001).

49. B. J. H. Van Os, L. J. Lourens, F. J. Hilgen, G. J. De Lange, L. Beaufort, The formation of Pliocene sapropels and carbonate cycles in the Mediterranean: Diagenesis, dilution, and productivity. *Paleoceanography* **9**, 601–617 (1994).

50. L. Diester-Haass, C. Robert, H. Chamley, *Paleoproductivity and Climate Variations During Sapropel Deposition in The Eastern Mediterranean Sea* (1998).

51. A. Micallef et al., Land-to-sea indicators of the Zanclean megaflood. *Commun. Earth Environ.* **5**, 794 (2024).

52. C. Martin-Puertas, R. Tjallingii, M. Bloemsma, A. Brauer, Varved sediment responses to early Holocene climate and environmental changes in Lake Meerfelder Maar (Germany) obtained from multivariate analyses of micro X-ray fluorescence core scanning data. *J. Quaternary Sci.* **32**, 427–436 (2017).

53. J. Laskar, A. Fienga, M. Gastineau, H. Manche, La2010: A new orbital solution for the long-term motion of the Earth. *A & A* **532**, A89 (2011).

54. L. J. Lourens et al., Evaluation of the Plio-Pleistocene astronomical timescale. *Paleoceanography* **11**, 391–413 (1996).

55. C. Pierre, A. Caruso, M.-M. Blanc-Valleron, J. M. Rouchy, F. Orzsag-Sperber, Reconstruction of the paleoenvironmental changes around the Miocene-Pliocene boundary along a West-East transect across the Mediterranean. *Sediment. Geol.* **188–189**, 319–340 (2006).

56. D. Gallego-Torres et al., Productivity patterns and N-fixation associated with Pliocene-Holocene sapropels: Paleoceanographic and paleoecological significance. *Biogeosciences* **8**, 415–431 (2011).

57. S. Ramondenc et al., An initial carbon export assessment in the Mediterranean Sea based on drifting sediment traps and the underwater vision profiler data sets. *Deep Sea Res. Part I Oceanogr. Res. Pap.* **117**, 107–119 (2016).

58. A. Guyennon et al., New insights into the organic carbon export in the Mediterranean Sea from 3-D modeling. *Biogeoscience* **12**, 7025–7046 2015).